# Effects of polymer coating mechanics at solid-electrolyte interphase for stabilizing lithium metal anodes

Zhuojun Huang,<sup>1,†</sup> Snehashis Choudhury,<sup>2,†</sup> Neelima Paul,<sup>3,†</sup> Johannes Helmut Thienenkamp,<sup>4</sup> Peter Lennartz,<sup>4</sup> Huaxin Gong,<sup>2</sup> Peter Müller-Buschbaum,<sup>3,5</sup> Gunther Brunklaus,<sup>4</sup> Ralph Gilles,<sup>3,\*</sup> & Zhenan Bao<sup>2,\*</sup>

- <sup>1</sup>Department of Materials Science and Engineering, Stanford University, Stanford, CA 94305.
- <sup>2</sup> Department of Chemical Engineering, Stanford University, Stanford, CA 94305.
- <sup>3</sup> Heinz Maier-Leibnitz Zentrum (MLZ), TU München, Lichtenbergstr. 1, 85748 Garching, Germany
- <sup>4</sup> Institute of Energy and Climate Research, IEK-12: Helmholtz-Institute Münster (HI MS) Ionics in Energy Storage, Münster, Germany
- <sup>5</sup> Lehrstuhl für Funktionelle Materialien, Physik-Department, TU München, James-Franck-Strasse 1, 85748 Garching, Germany
- <sup>†</sup> Z.H., S.C., and N.P. contributed equally to this work.

#### **Abstract**

Lithium metal batteries are next generation energy storage devices that rely on the stable electrodeposition of lithium metal during the charging process. The major challenge associated with this battery chemistry is related to the uneven deposition that leads to dendritic growth and poor coulombic efficiency. A promising strategy of addressing this challenge is utilizing a polymer coating on the anodic surface. While several works in the past have evaluated polymer coatings, the requirement for polymer design is still unclear. In this work, we specifically investigate the effect of polymer dynamics on lithium metal deposition. We design electrolyte (solvent) blocking perfluoro polyether polymer networks with evenly spaced H-bonding sites of various strengths, resulting in significant differences in the molecular ordering, as analyzed by x-ray scattering measurements. The differences in the H-bonding strength directly impacted the mechanical properties of these materials, thus providing a controlled set of samples with a range of polymer dynamics for electrodeposition studies. Finally, a systematic evaluation of the lithium metal electrodeposition quality with these polymers as anodic coating showed that polymers with flowability or faster polymer dynamics exhibited higher coulombic efficiency. These experimental findings provide rational design principles of soft polymer coatings on lithium metal anodes.

<sup>\*</sup>e-mail: Ralph.Gilles@frm2.tum.de; zbao@stanford.edu

#### Introduction

The current accelerating climate change and global warming make it more pressing for deployment of renewable energy resources as well as electrification of transportation systems. In this regard, energy storage is an important link between energy generation and consumption. There have been significant interests over the past few decades to increase energy density of battery systems, wherein lithium-ion batteries (LIBs) have been the workhorse energy storage devices.(Whittingham, 2012) However, with the growing demand for energy usage, the LIBs fall short in delivering the ever-increasing needed high energy density. One pathway of increasing the energy density is replacing the graphitic anode in a LIB with a lithium metal in a so-called lithium metal battery (LMB).(Dunn, Kamath and Tarascon, 2011; Liu et al., 2019) The anode-specific capacity of an LMB is in theory ten-times that of LIB and it also enables the utilization of lithium-free high capacity cathodes like sulfur or oxygen, leading to even higher energy densities. However, commercialization of LMBs requires stable electrodeposition of lithium metal after repeated charging/discharging cycles. It is known that at an electrodeposition rate above the diffusion-limited current density, the anion concentration near the electrode would drop to zero leading to unstable or dendritic electroplating of metals.(Brissot, Rosso and Lascaud, 1999; Rosso et al., 2001; Bai et al., 2016) However, this finding ignores the reactivity of the metal electrode as well as the chemical heterogeneity of the electrolyte-electrode interfaces due to solid electrolyte interphase (SEI) formation.(Lin,

Liu and Cui, 2017) Such idealistic assumptions are clearly violated in practical metal batteries due to intrinsic surface defects of the metals and parasitic reactions between electrodes and electrolytes (also in sodium, aluminum or magnesium metal anodes) resulting in abrupt battery-failure even at low current densities.(Cheng *et al.*, 2017; Zheng *et al.*, 2020)

The strategies associated with stabilizing such reactive metals go beyond the electrochemical fundamentals to the realm of material science, polymer chemistry and nanotechnology. Such approaches can be well captured in two broad categories of modified electrode-electrolyte interphases(Ding et al., 2013; Miao et al., 2014; Choudhury et al., 2017; Tu et al., 2017; H. Zhang et al., 2018; Lopez et al., 2018; Gao et al., 2019, 2020) and hybrid electrolyte design(Pieczonka et al., 2013; Zhang et al., 2017; Li et al., 2018; Ren et al., 2018; Zeng et al., 2018; Amanchukwu et al., 2019). Several groups have implemented artificial protective layers on anode surfaces using polymer fibers(Lopez et al., 2018; R. Zhang et al., 2018), inorganic nanoparticles(Choudhury et al., 2016; Kim et al., 2016) and metal (Choudhury et al., 2017; Liang et al., 2017; Tu et al., 2018) to prevent the continuous exposure of native metal with the reactive electrolytes. In addition, halogen(Choudhury et al., 2018; Suo et al., 2018) and sulfur(Pires et al., 2015) based chemical additives as well as ether-based electrolytes(Qian et al., 2015; Miao et al., 2016; Amanchukwu et al., 2020) are known to breakdown at the interface to form a compliant protective layer. On the other hand, hybrid electrolyte architectures such as superionic inorganics(Croce,

Sacchetti and Scrosati, 2006; Zheng, Tang and Hu, 2016; W. Liu *et al.*, 2017; Chen *et al.*, 2018) or crosslinked polymer networks(Choudhury *et al.*, 2015, 2019; Hu *et al.*, 2017) have been shown to suppress effectively the instabilities due to confinement of electrodeposition in nanoscale ionic channels or by ultra-high compressive forces.

A recent unique strategy of addressing the anode-specific instabilities is designing a polymer coating for the lithium metal anode to regulate the localized ion transportation with the goal to produce homogenous growth of metal anodes. (Zheng et al., 2016; Tu et al., 2017; Lopez et al., 2018, 2019; Gao et al., 2019) There have been different polymer architectures evaluated to serve as protective coating on the lithium metal anode, including, single-ion conductors(Huang et al., no date; Tu et al., 2017; Yu et al., 2019), polymer composites(Choudhury et al., 2016), self-healing polymers(K. Liu, Pei, Lee, Kong, Liu, Liu, Liu, P. Hsu, et al., 2017; Yu et al., 2019), and crosslinked elastomers(Choudhury et al., 2019). Specifically, self-healing polymers and flowable polymers resulted in uniform deposition of lithium metal in previous studies.(Huang et al., no date; Lopez et al., 2018, 2019; Kong et al., 2020) However, it was unclear how polymer dynamics impact lithium metal deposition in a well-controlled polymer coating where polymer dynamics is the only variable.

In this work, we analyze the lithium metal deposition based on effects of mechanical properties of a series of polymer coating materials with the same polymer backbone and evenly spaced H-bonding sites of systematically tuned strength. We hypothesize that

dynamic polymer architectures may prevent morphological instabilities during electrodeposition compared to rigid polymers and covalently crosslinked elastomers, when used as artificial interfaces between the electrode and electrolyte. The hypothesized working mechanism of the dynamic polymer coatings is potentially from the spontaneous adaptation of the polymer and maintain uniform ion transport, due to its dynamic roughening nature, in response to the electrode during electrodeposition.(Zheng et al., 2016) If the polymer coating is flowable, it may rearrange, and cover regions considered as 'hotspots' (uneven deposits) on the surface of the lithium metal electrode. By shielding these 'hotspots' from successive Li<sup>+</sup> ions, the proposed coating can achieve uniform Li deposition. Previous experimental and theoretical works have shown the concept of more uniform lithium metal deposition with flowable polymer coating.(Zheng et al., 2016; Kong et al., 2020) However, there was a lack of a wellcontrolled polymer coating system, where the polymer mechanics is the only changing parameter. In this study, we synthesize a series of polymers with the same polymer backbones having varying strength of hydrogen bonding (H-bond) sites that render systematic evaluation of the electrodeposition stability in relation to the mechanical properties feasible.

#### **Results and Discussion**

<u>Polymer Design and Characterization</u>

To directly correlate the effect of polymer dynamics/mechanics on the electrodeposition, we design polymer networks having the primary backbone of perfluoropolyether (PFPE) and adjusted the strength of H-bonding units to vary the mechanical properties. PFPE backbone is chosen for its chemical inertness and minimal swelling with liquid electrolyte solvents, which constitutes a major cause of lithium metal degradation. (Yang et al., 2021) Specifically, we synthesized polymers comprising of various contents of non-covalent Hbond interactions using polymerization of flexible PFPE polymer (having a low glass transition temperature, Tg) with urea linkages formed using diisocyanate units. Due to the more polar nature of the urea groups, we expect that they eventually aggregate into hard domains. Two types of urea units were utilized in this work, that is, isophrone (I) and bismethylene diphenyl units (M), as shown in figure 1a. These units are known to afford different strength of H-bonds in the corresponding supramolecular polymer network.(Cooper et al., 2020) The diphenyl units in the M block have the ability to form pi-pi stacking and also strong quadrupolar H-bonds, while the *I* units are known to form weaker H-bonds due to steric hindrance from the isophrone units and low symmetry of the molecule.(Cooper et al., 2020)

The synthesized polymers were characterized with solid-state <sup>1</sup>H-Nuclear Magnetic Resonance (<sup>1</sup>H-NMR) and the attributions of several hydrogen groups were shown in figure 1b. Due to the viscous nature of the M0I1 sample, the solid-state NMR experiment cannot be performed on it without severe risk of hardware damage. We assigned the two

peaks around 5 ppm to the two N-Hs in the I-units, which reside in slightly different chemical environments. These two peaks were missing in the M110 NMR spectrum as expected, and their intensity increased as the I ratio increased (from M3I1 to M1I3), matching the proposed synthesis scheme. We also attributed the single peak between 7.2 and 8 ppm to the N-H from the M units, while the peak at 4.3 ppm reflects the -CH<sub>2</sub>-Oconnection formed when the alcohols on the PFPE chains reacted with the isocyanates in the linker units. Interestingly, the chemical shifts of -N-H protons involved in the Hbonding units for both M and I units all moved to lower ppm values as the amount of M units increased. Typically, such a shift is an indication of weakening of the Hbonding, (Paul et al., 2018) which is unexpected as M units are known to form stronger Hbonding than I-units. We hypothesized that although individual M units form stronger and more stable H-bonds than I units, the reduced mobility from polymers with more M units may have limited their ability to yield conformationally more stable hydrogen bonds, which resulted in the reduced hydrogen bonding strength as more M units are incorporated.(Liu et al., 2018) For the hydrogen groups that are not involved in H-bonds, like the -CH2-O-, their chemical shifts remained unchanged at different linker compositions.

To characterize the mechanical properties and dynamics of these polymers, we performed frequency dependent oscillatory shear measurements to analyze the mechanical and molecular properties of the supramolecular polymers. Specifically, we

utilized a strain of 1% at different temperatures and finally performed Time-Temperature Superposition (TTS) to obtain the rheology data at a wider frequency range. The high frequency regime corresponds to the elastic behavior of the material, while the low frequency range corresponds to the viscous effects. Briefly, the storage modulus (G') and loss modulus (G") denote the solid and liquid characteristic of the materials. If G' is larger than G", the material exhibits elastic solid-like behavior. It can be seen from figure 1c that the polymers with higher M unit content (M1I0 and M3I1) show solid-like characteristics at the high frequency regime, while other polymers show viscous liquid-like behavior. In fact, at a 50% M unit in the polymer (M111) there is a crossover from viscoelastic liquid to viscoelastic solid, which can be attributed to the gel-point for these dynamic H-bonded polymer networks. Notably, polymers with higher M content have higher G' and G" across the frequency range, indicating higher mechanical rigidity. We discussed the mechanical property of these polymers after soaking in electrolytes in the following sections.

# Morphological Analysis using SAXS/WAXS

Small-angle x-ray scattering (SAXS) and wide-angle x-ray scattering (WAXS) measurements were performed on all polymer samples to extract information on their inter-block spacing and molecular morphology as a function of H-bond strength and temperature. Since all polymers consist of a fluorinated PFPE backbone interlinked with

non-fluorinated block units, the large electron density difference between the backbone and the block units is expected to result in a scattering peak in the SAXS profile at a Q (Qscattering vector, defined as  $Q=4\pi \cdot \sin(\theta/2)/\lambda$ , where  $\theta$  is the scattering angle and  $\lambda$  is the wavelength) position corresponding to the distance between the PFPE block units. Combining WAXS with the SAXS regions, the measurable Q range is extended to cover a wide range of length scales from sub nanometer to tens of nanometers. Not only the inter-block unit distances but also their orientation, in virtue of their being conducting units, are expected to affect the overall mechanics and in turn, the coulombic efficiency of the polymer. If the orientation of ionic conducting units is such that they are parallel to the electrode, then the conductivity of the polymer is expected to be low because these units will not contribute to ion transport between electrodes. On the other hand, if these conducting units are oriented perpendicular to the electrode, then the conductivity of the polymer is expected to be higher. In case of polymers, where the conducting units are randomly arranged, one generally expects 2/3rd of the maximum possible conductivity from diffusion models.(Singh et al., 2007)

The 2D WAXS data for all five polymer samples are shown in figure 2a-j for measurements at temperatures 30°C and 90°C. As some rings seemed anisotropic, azimuthal cuts were taken along the ring maximum for each polymer and temperature and were plotted in the supplementary information (supplementary Figure 1) to check

for anisotropy and directions of preferred orientations. An anisotropic ring is an indication of preferential orientation of grains or chain conformations because anisotropic azimuthal intensity distributions in WAXS patterns are typically due to texture. As the amount of order in alignment decreases, azimuthal broadening occurs, and therefore a randomly oriented sample results in a 2D pattern with an isotropic diffraction ring.

At 30°C, polymers M0I1, M1I3 and M3I1 showed isotropic WAXS rings, i.e. the radially integrated intensities are homogeneous over the complete azimuthal angular range from 0° to 360°. Thus, it could be concluded that urea units connected by H-bonds in these polymer samples are nearly randomly oriented or with randomly oriented conformations. At 90°C, the rings remain isotropic for polymers M0I1 and M1I3, but become anisotropic for the polymer M3I1, where the content of M unit is comparatively higher. On the other hand, polymer M1I0 (Figure 2e), where the content of the M units is the highest, the WAXS rings are prominently anisotropic at all temperatures.

Interestingly, for polymer M1I1 with equal content of M and I units, a slight anisotropy is also observed at all temperatures. Thus, at 30°C, which is close to ambient temperature, polymer M1I1 and polymer M1I0 had prominent preferred orientations and the rest of the polymers had no preferred orientations. Such preferred orientations typically arise from strain or texture effects in the sample. Here, it is due to anisotropy from local aggregations of urea units as confirmed from AFM images of these samples

(supplementary Figure 2), where fiber-like structures are observed in the samples where content of M units is high. As fibers are lying parallel to the substrate surface, and SAXS/WAXS are sensitive to in-plane structures, we conclude that H-bonding direction is in-plane i.e. parallel to substrate surface. In Figure 2k, the azimuthally integrated 1D intensity cuts are plotted for all polymers at ambient temperature T= 30 °C as a function of the scattering vector Q. In the inset of Figure 2k, peak position and peak width were shown for each polymer. A prominent WAXS peak was present at the position corresponding to the rings in the 2D images. All peaks were fitted using a Voigt peak profile function to extract the precise peak position and peak broadening. One-dimensional WAXS and SAXS data for polymer M1I3 along with the fits are displayed in supplementary Figure 3. Supplementary Table 1 showed the results of the fits for this polymer. In supplementary Table 2, results of fittings of WAXS and SAXS peaks at 30°C for all polymers were shown. Depending on the polymer, the peaks were located at scattering vector Q values ranging from 11.58 nm<sup>-1</sup> for polymer M1I0 to 12.05 nm<sup>-1</sup> for polymer M1I3. These correspond to a prominent periodic length spacing of 0.54 nm for polymer M1I0, and 0.52 nm for polymers M0I1, M1I3 and M3I1. These periodic length spacing are of the same order of magnitude as the expected urea-urea stacking distances (0.45 nm) for the hydrogen-bonded urea groups.(Cooper et al., 2021)

As the position of the WAXS peak is at very similar values for all polymers, we concluded a similar chain packing density of hydrogen-bonded urea groups for these polymers.

Temperature dependence of this peak is expected to reveal changes in average distances between adjacent chains at these length scales and could be extracted from peak positions and broadening. In Figure 2I, these are plotted exemplarily for polymer M1I3, which shows the most prominent changes in the 2D WAXS data as a function of Q. Upon temperature increase, the intensity of the WAXS peak gradually decreases, slightly shifts from 12.05 nm<sup>-1</sup> towards 11.49 nm<sup>-1</sup> and broadens from 4.66 nm<sup>-1</sup> to 4.93 nm<sup>-1</sup>. The observed increase in the spacing from 0.52 nm to 0.55 nm, and peak broadening at higher temperatures could be due to kinetically induced effects such as extended chain lengths and disordered chain conformations including slight orientation changes.

#### Polymer nanostructure

The radially symmetric or isotropic SAXS rings, seen in 2D data of each polymer in figure 3 a-j, suggest that all polymer samples consist of randomly oriented nanostructures in this length scale. The scattering contrast between adjacent fluorinated and non-fluorinated block units is responsible for the appearance of the SAXS ring in the region Q from 1.62 nm<sup>-1</sup> to 1.34 nm<sup>-1</sup>, shifting to lower Q position upon increase in the content of M units. These Q positions correspond to a characteristic length spacing of 3.86 nm for polymer M0I1 and 4.67 nm for polymer M1I0, which seems a reasonable length for the spacing between the above-mentioned block units (see polymer structures in Figure 1a).

Figure 3k shows 1D SAXS profiles for all polymers at 30 °C. The SAXS peak for the most-solid like or rigid polymer M1I0 located at Q = 1.34 nm<sup>-1</sup> is the narrowest (0.44 nm<sup>-1</sup>). For the other polymers, the peak broadens with decreasing content of M units and is the broadest (0.78 nm<sup>-1</sup>) for the most-liquid-like polymer M0I1, whose Q peak position is located at 1.62 nm<sup>-1</sup>. The shift of the primary scattering peak to higher Q values results from a reduced spacing between adjacent fluorinated block units with decreasing content of M units whereas peak broadening is caused due to a larger variation in spacing between the units.

In Figure 3I, as an example we show the temperature dependence of the SAXS profile for polymer M1I3. We note a decrease in peak intensity and broadening from 0.68 nm<sup>-1</sup> to 0.95 nm<sup>-1</sup> on temperature increase from 30 °C to 90 °C. Thus, also at larger length scales, the higher polymer dynamics result in a broadened distribution of the inter block spacing. The peak position also shifts from 1.52 nm<sup>-1</sup> to a higher Q value of 1.55 nm<sup>-1</sup> after heating, which implies a reduction in length spacing from 4.10 nm at 30 °C to 4.03 nm at 90 °C for polymer M1I3. A similar trend with temperature has also been observed by Balsara and group for PFPE<sub>E10</sub>-Diol systems(Chintapalli *et al.*, 2017).

In summary, the above WAXS characterizations suggest that there is a similar chain packing density for all polymers at 30 °C. The polymers M0I1, M1I3, M3I1 show no preferred orientations, polymer M1I1 and polymer M1I0 shows prominent preferred orientations. At 90 °C, polymers with lower contents of the M units (M0I1, M1I3) showed

no preferred orientations, whereas polymers with higher contents of M units (M1I1, M3I1 and M1I0) showed prominent preferred orientations.

From SAXS investigations at 30 °C, we extract the smallest spacing of 3.86 nm between fluorinated block units for polymer M0I1 and the largest spacing of 4.67 nm for polymer M1I0, which is in good agreement with the polymer structures. On temperature increase, the polymer dynamics is enhanced, resulting in a broadened distribution of the inter block spacing and a slight decrease in the spacing between the fluorinated units (e.g. from 4.10 nm at 30 °C to 4.03 nm at 90 °C for polymer M1I3).

# Interactions between polymers and lithium salt

To understand how the polymer interacts with lithium ion, we mixed lithium bis(trifluoromethanesulfonyl)imide (LiTFSI) salt into the polymers (molar ratio Li: linker unit = 1:1). The Fourier transform infrared (FTIR) spectrum of the M0I1 and M1I0 were taken before and after the addition of LiTFSI salt, and the region corresponding to C=O and N-H stretching were shown in figure 4a, b. Before salts were added to the polymer, we observed the C=O stretching of M1I0 and M0I1 at 3336 and 3347 cm<sup>-1</sup>. For both bond stretching modes, the peak locations are consistent with literature reported values.(Gasperini *et al.*, 2019) When lithium salts were added to the system, Li<sup>+</sup> forms Lewis acid complexation with the basic carbonyl oxygen site, which caused the lengthening of the C=O bond and thus the observed ~10 cm<sup>-1</sup> red shift.(Roberts and

Jenekhe, 1991) This interaction weakens the H-bonds, and the partially unbounded N-H group become shortened, resulting in the 40-50 cm<sup>-1</sup> blue shift (Supplementary figure 4). Previous literatures have reported an 88 cm<sup>-1</sup> blue shift of the N-H in a H-bond between bounded and unbounded state.(Gasperini *et al.*, 2019) We observed a smaller blue shift upon the salt addition, indicating that Li<sup>+</sup>'s interaction with the H-bonds does not completely disassociate them.

We further characterized the mechanical property of the polymers after soaking in the carbonate electrolyte, and the rheological frequency sweeps of the polymer M0I1, M3I1 and M1I0 were shown in figure 4c-e. The tan(delta) and the storage modulus (G') at 10 rad/s of the polymers before and after 2 hours of soaking were labelled in the graph. After soaking, the G' decreased and the tan(delta) increased, indicating softening of the polymer network. Notably, the M1I0 polymer maintained its solid nature at the 1-100 rad/s frequency range, with no crossover between G' and G" observed, while M3I1 polymer showed viscoelastic behavior with a crossover frequency at 10 rad/s. We further soaked the M1I0 polymer in the carbonate electrolyte for 12 hours, and the G'/G" frequency sweep overlapped with the ones from 2 hours of soaking (supplementary figure 5), indicating that 2 hours of soaking time was sufficient to reach steady state. Overall, the trend of the polymer's mechanical property remained the same, i.e. the dynamics reduced as the M unit ratio increased. This trend was maintained after the polymers were soaked in electrolyte.

## **Electrodeposition Stability**

We analyzed the efficacy of these polymers in preventing lithium dendrite growth when used as an anodic coating. Specifically, we measured the coulombic efficiency of lithium deposition/stripping in Lil | Cu cells, where the copper electrodes were coated with the polymer solution using spin coating method. In this measurement, a fixed amount of lithium (5 mAh/cm<sup>2</sup>) was deposited onto the copper electrode, followed by repeated stripping and plating for shorter timeframes (2 hours at 0.5 mA/cm<sup>2</sup>). Thereafter, the amount of lithium remaining from the copper electrode was quantified for obtaining the coulombic efficiency of electrodeposition. The electrolyte utilized in this experiment was 1M LiPF<sub>6</sub> in EC/DEC with 10 % FEC. Figure 5a shows on left compared with the coulombic efficiency of the different polymer coatings with varying ratios of M units compared with the bare electrode, and the voltage curve of these coulombic efficiency measurements were shown in supplementary figure 6. It is seen that the coulombic efficiency (CE) is higher for the polymer-coated copper compared to the bare. It is important to note here that previous reports on polymer coatings have been shown to be effective in only ether-based electrolytes and not in carbonate-based systems which are more desirable for high voltage batteries. (Lopez et al., 2018) Thus, improved CE with the current polymer coating is interesting and encouraging. The results also show an interesting trend of the CE with respect to the polymer structure and mechanical

properties. It is seen that lower content of the M units (M0I1, M1I3, M1I1, M3I1) in these polymers exhibited higher CE compared to higher M unit containing polymers (M1I0). In other words, it is apparent that the coulombic efficiency is higher for the viscous liquid-like polymers in comparison to the more rigid solid-like polymers. It appears that the polymer coatings with faster dynamics enabled more stable deposition, which is a deviation from the long–standing concept in solid electrolytes which states that high modulus is important to prevent dendrites.(K. Liu, Pei, Lee, Kong, Liu, Liu, Liu, P. chun Hsu, *et al.*, 2017) Similar observations have also been reported in our prior studies using self-healing and flowable polymer coatings on lithium anode.(Zhang *et al.*, 2017) Furthermore, simulation work from Qin et al. also found that viscoelastic polymer coating can promote stable deposition of Li while solid-like polymer layer can lead to unstable and uneven lithium deposition.(Kong *et al.*, 2020)

We further examine the morphology of lithium deposition on the copper electrode with and without polymer coating (Figure 5b). We plated 1 mAh/cm² of lithium on the copper electrode (with or without coating) at a current density of 0.5 mA/cm². The cell was disassembled and the Cu electrode was rinsed with DME (dimethoxyethane) for 30 seconds to remove excess salt and polymer before imaging with SEM. For cells with no polymer coating, we observed needle-like dendritic deposition, consistent with the lithium deposition structure in carbonate electrolyte. When a layer of viscoelastic

polymer coating was applied to the Cu electrode (M0I1 and M1I3), the underlying polymer lithium deposition was smooth and homogenous. As the modulus of the coating increased and with slower dynamics (from M1I3 to M1I1), residual polymer remains between deposited lithium after washing. A further increase in modulus (M3I1 and M1I0) led to irregular lithium deposition protruding out of the polymer coating. We noted that the M3I1 showed more charging under SEM than the M1I0, which was due to more dendritic lithium deposition penetrating the polymer layer for the M1I0 coating. Overall, we found a consistent correlation between homogenous lithium deposition and higher coulombic efficiency measurements (figure 5a). Among the five coatings we investigated, M1I3 had the highest CE, and M1I0 had the lowest CE. Beyond cycling performance, these two polymers also showed the most distinct deposition morphologies: For the M1I3 coating, lithium deposited underneath the polymer as large homogeneous chunks, and for the M1I0 coating, lithium deposited through the polymer coating as irregular dendritic structures. Based on these investigations, we focused on M1I3 and M1I0 as the two most representative polymer coatings for further characterizations.

We further characterized the coating's coverage of the deposited lithium for the M1I3 (viscoelastic) and M1I0 (solid-like) polymer without washing the electrode. Supplementary figure 7 showed the tilted and cross section SEM of a M1I3 coating covered Cu electrode with 1 mAh/cm² of lithium deposited: The M1I3 polymer coating homogeneously covered the uniform deposited lithium. Supplementary figure 8 showed

the tilted SEM of a M1I0 coating covered Cu electrode. Regions of the electrode remained covered with the polymer coating, while other regions of the electrodes had irregular lithium deposition that ruptured the coating layer. Overall, through a series of top view, cross section, and tilted SEM images of deposited lithium, we demonstrated that a viscoelastic polymer coating is important for maintaining a homogeneous coverage of the electrode and promoting uniform lithium deposition morphology.

The cycling (50 cycles) behaviors of the coatings were also examined in Lill Cu cells, and their coulombic efficiency over cycles were plotted in figure 6a. To quantify their performance, the stabilized average CE (cycles 30-50) and their STD (standard deviation) were plotted in figure 6b. Overall, the LillCu cells with the M1I3 polymer coating has the highest average CE (95.7%) with the lowest STD, indicating stable cycling performance. For the case of no polymer coating, the average CE was 94.2%, with a large (>1%) STD. When the Cu electrodes were coated with the M1I0 polymer coating, the CE was improved (94.6%), but the STD remained large. The average CE and STD of a repetition sets of LillCu cells were plotted in supplementary figure 9, and similar trends was observed. We found the CE and STD of the cells to be consistent with literature reported values on carbonate electrolyte.(Chen et al., 2020) Overall, the cycling results indicated that a viscoelastic polymer coating (M1I3) can promote more stable longer-term operation of the battery. Table s3 compared different literature strategies to improve the CE in carbonate electrolyte at a current density 0.5 mA/cm<sup>2</sup> and capacities 1 mAh/cm<sup>2</sup>. Our work on using a PFPE based polymer coating (M1I3) has a higher CE than 95%, which renders it among one of the high-performance strategies in literature.(Yu *et al.*, 2019)

The median lithium deposition voltages of each cycle were also shown in figure 6c, where the cells with polymer coatings showed higher overpotential (~35 mV) than the cells with bare electrodes (~20 mV). We attribute the increased overpotential to the slower Li<sup>+</sup> transport through polymer coatings compared to bare electrodes. By soaking the polymer in EC/DEC electrolytes for 2 hours and performing EIS measurement on it afterwards, we found that the M1I3 and M1I0 polymers have similar room temperature ionic conductivities (3.3-3.5×10<sup>-6</sup> S/cm). Their Nyquist plots were shown in supplementary figure 10. Since M1I3 and M1I0 have largely different M to I ratio, we expected the overpotential to not vary significantly as a function of polymer composition, and we can attribute their distinctions in electrochemical performance to the mechanical property differences among the coatings.

Because both M1I3 and M1I0 polymers contained the same PFPE solvent blocking units, we want to analyze how the polymer coating impacted the SEI (solid electrolyte interphase) composition after 50 cycles. The X-ray photoelectron spectroscopy (XPS) were

performed on the sample and the C1s spectra of the samples were shown in figure 6d. With a layer of M1I3 coating added, the SEI layer showed less signal (74 %) from C-C and C-H bonds (resulting from EC electrolyte solvent breakdown), comparing to the no coating control (82%). The solid-like M1I0 coating showed less resistance towards solvent decomposition, with 80% of the signal attributed to solvent breakdown. We reasoned that the viscoelastic nature of the M1I3 polymer can maintain a homogenous coverage of the deposited Li metal over cycles, while the solid-like M1I0 polymer may have small ruptures, exposing the Li metal directly to the electrolyte, which results in electrolyte decomposition, consistent with previous simulation findings(Kong *et al.*, 2020) and our SEM images. These findings on CE, lithium deposition morphology, deposition overpotential and SEI composition clearly indicate that the soft polymer on the surface of anode drives the stability of electrodeposition.

#### Conclusion

We designed a series of polymers comprising of a perfluoropolyether (PFPE) soft block and urethane-based hard blocks. The PFPE units provide flexible polymer backbones, while the urethane units can be used to tune polymer network rigidity and stiffness through H-bonds. We specifically utilized two different urethane chemistries having low and high H-bonding strengths. Various combination of these two urethane units resulted in a series of polymers with different levels of dynamics. We utilized small- and wide-

angle X-ray scattering (SAXS/WAXS) analysis to determine the microstructures and observed that the more M units containing polymers with higher H-bonding strength have a narrower distribution and more ordered structure, while the lower H-bonding strength and more I units containing polymers have broader distribution and comparatively reduced inter-block spacings. The differences in the molecular structure result in similar variation of the mechanical properties as observed in rheological measurements. The polymers with high ratio of M units behave like viscoelastic solids, while the polymers with more I units act as viscoelastic liquid. We finally analyzed the effect of molecular/mechanical properties on the lithium metal electrodeposition morphology, when these polymers were used as coatings on the lithium anode. It was observed that the flowable/softer polymer coatings enabled higher coulombic efficiency (CE) of electrodeposition, while the more rigid polymers resulted in poorer CE. This work provides understanding of the design principles for polymer coatings for lithium metal deposition in relation to their mechanical strength. Further understanding of the underlying mechanisms are being developed.

#### Acknowledgement

The work was supported by the US-German joint collaboration on "Interfaces and Interphases In Rechargeable Li-metal based Batteries" supported by the US Department of Energy (DOE) and German Federal Ministry of Education and Research (BMBF, grant 13XP0224A). Support from the Assistant Secretary for Energy Efficiency and Renewable

Energy, Office of Vehicle Technologies of the U.S. Department of Energy is also acknowledged. Part of this work was performed at the Stanford Nano Shared Facilities (SNSF), supported by the National Science Foundation under award ECCS-1542152. Z.H. and S.C. thanks W.H., C.C. and J-C.L for helpful discussion and experimental assistance regarding the hydrogen bonding discussion. P.M.-B. acknowledges the financial support from the Deutsche Forschungsgemeinschaft (DFG, German Research Foundation) via grant Mu 1487/38-1. The work presented here has received funding from the German Federal Ministry of Education and Research (BMBF) under the grant number 03XP0224C.

## **Materials and Methods**

## **Synthesis of PFPE polymers**

Detailed synthesis methods of the PFPE polymers with different amounts of M and I linker ratios were shown in the supplementary information and supplementary table 3.

Small-angle X-ray scattering (SAXS) and wide-angle X-ray scattering (WAXS)

Small-angle X-ray scattering (SAXS) and wide-angle X-ray scattering measurements (WAXS) were performed using a Ganesha 300XL SAXS-WAXS system (SAXSLAB ApS, Copenhagen/Denmark) at TUM, equipped with Cu anode (0.154 nm) and a movable 2D Pilatus 300 K detector with pixel size  $172 \times 172 \mu m$ . For SAXS, the detector was positioned at a sample-detector distance corresponding to 390 mm and exposure time of 7200 s was used to acquire data. For WAXS, the sample-detector distance was 99 mm, and the exposure time was 3600 s. Each polymer sample was carefully placed between two mica windows and sealed in custom-designed steel holders with a rubber O-ring. These holders were mounted on a Linkam HFSX350 stage, equipped with a water-cooled jacket, annealed followed by 15 minutes of equilibration at each temperature before starting the respective measurements at that temperature. The temperatures used were 30°C, 50°C, 70°C and 90°C. We chose a broad temperature range from 30°C to 90°C because this range is relevant for designing room temperature as well as high temperature Li-metal based batteries using polymer electrolytes. From the reduced 2D SAXS/WAXS data, the azimuthally averaged scattering intensities (I) were extracted and were plotted as a function of the scattering vector (Q) in a 1D plot. The inter block unit distance, d, was calculated using the formula  $d = 2\pi/Q_{peak}$ , where  $Q_{peak}$  was the value of the Q vector at the maximum of the scattering peak in the 1D SAXS plot.

## Rheological Measurements

The rheological measurements were done using an ARES G2 rheometer (TA Instruments) with an advanced Peltier system (APS) at variable temperatures. An 8mm diameter parallel plate geometry was used for all measurements. The time-temperature-superposition for the polymer samples were also done in the linear viscoelastic region between the frequency range of 100 rad/sec to 0.1 rad/sec between 0 °C to 125 °C. The obtained frequency sweep curves were shift horizontally and vertically, with the data at 25 °C as reference to obtain the master curves.

#### Solid-State Nuclear Magnetic Resonance

All the <sup>1</sup>H MAS experiments were performed at a 14.1 T Bruker Avance III HD device with a Larmor frequency of 600.8 MHz using a commercially available Bruker double resonance probe with 3.2 mm MAS rotors spinning at 15 kHz. All spectra were recorded with 100 kHz rf nutation frequency (2.5 µs 90° pulse length), averaging 64 transients at a repetition time of 16 s. The lower and upper part of the 3.2 mm MAS rotors were filled with PTFE tape to reduce the volume expansion of the viscoelastic polymers due to frictional heating at rotation frequencies of 15 kHz.

#### **Battery Testing and SEM Analysis**

All electrochemical tests were done using 2032-type coin cells (MTI). All cell fabrications were done in Argon-filled glovebox. 750 μm Li foils (Alfa Aesar) and 6 μm Tough Pitch Copper foils (MTI) were used for Li | copper cells. Celgard 2325 separators were used for all battery configurations. For the polymer coated copper electrodes were made using spin-coating of the polymer solution. Specifically, the polymer samples were dissolved in TFB (0.1 g/ml) by heating at 80 °C. This solution was spin-coated onto 1cm² copper electrodes at 1000 rpm for 1minute. Finally, the electrodes were dried at 100 °C overnight under vacuum before transferring into an Argon filled glovebox and re-baked at 80 °C for 12 hours for next steps. By using the above coating and processing method, the thickness of the polymers coated on the Cu electrode was determined as ~1 μm using a profilometer. The electrolyte utilized for the electrochemical measurement is: 1M LiPF6 in EC/DEC(10% FEC). In all coin cells, 80μl of electrolyte was utilized.

For coulombic efficiency measurements, and SEM analysis studies, copper discs (1 cm²) were punched out and then coated with the polymers using the process mentioned earlier. In the coulombic efficiency (CE) measurements, the coated and uncoated copper electrodes were paired against lithium metal anode with a celgard-2500 separator. The short-term coulombic efficiency measurements were preceded by 10 charge and discharge cycles at a low current density of 0.02 mA/cm² between the voltages 0 to 1 V for pre-conditioning. Then, 5 mAh/cm² was deposited, stripped and redeposited before 5 cycles of plate-strip using 1 mAh/cm² capacity, and finally completely stripping the

deposited lithium from the copper electrode. The long-term coulombic efficiency measurements were preceded by 10 charge and discharge cycles at a low current density of 0.02 mA/cm2 between the voltages 0 to 0.5 V for pre-conditioning. Then, 1 mAh/cm2 of Li was deposited, stripped (to 0.5 V v.s. Li) for cycles at the current density of 0.5 mA/cm2.

The XPS profile was on Cu electrodes after 50 cycles of lithium strip and plating, collected with PHI VersaProbe 3 XPS probe with an Al K-alpha source. The surface was sputtered with Ar ion at 2 kV 1 uA on a 2 mm × 2 mm surface for 4 min before the measurements were collected. The signal was collected from a 0.2 mm x 0.2 mm area inside the sputtered area. The SEM (FEI Serion) analysis was done on a 1mAh/cm² deposited lithium on copper electrode at the first cycle after preconditioning.

Specifically, in these measurements, the coin cells were uncrimped inside the glovebox. The electrodes were rinsed using fresh DME before being placed in a sealed transfer vessel. All cycling tests were done at ambient conditions.

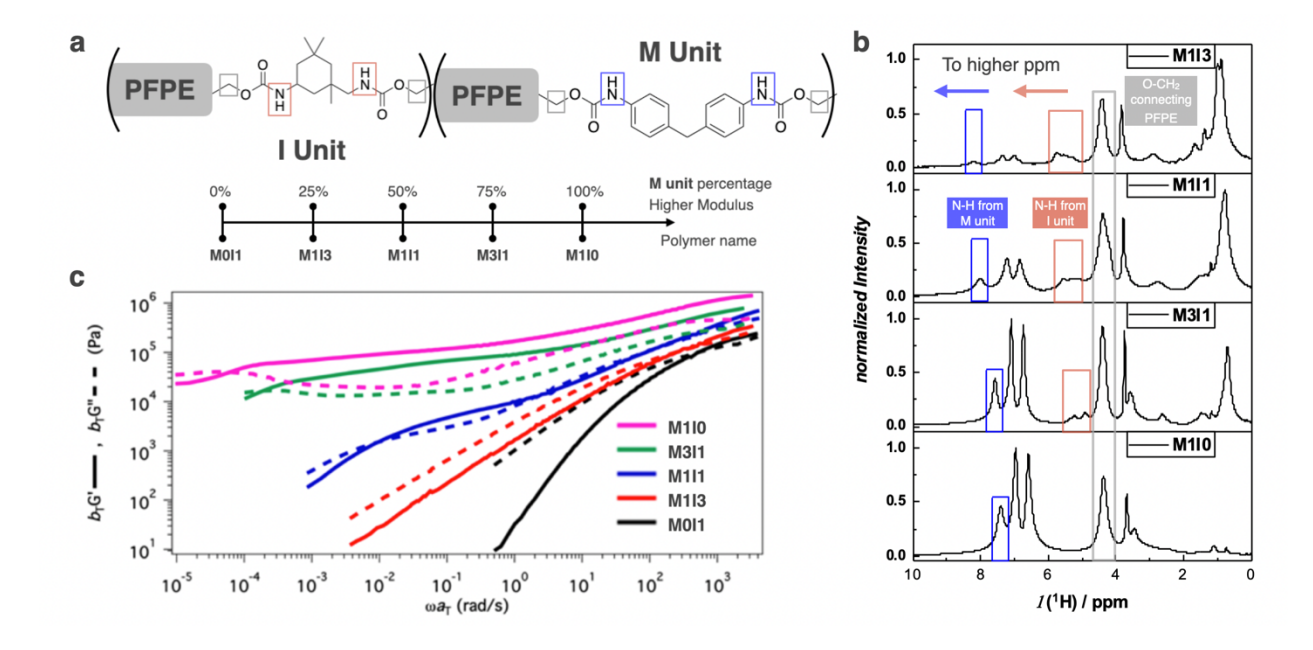


**Figure 1:** Polymers with different H-bond strength: **a**, structure of polymers used in this study. Here, PFPE block represents perfluoropolyether, which has a molecular weight of 4000Da; **b**, solid-state NMR measurement of different polymers with different hydrogen peaks boxed; **c**, frequency dependent storage and loss modulus of polymer samples obtained using oscillatory shear measurements at 25°C.

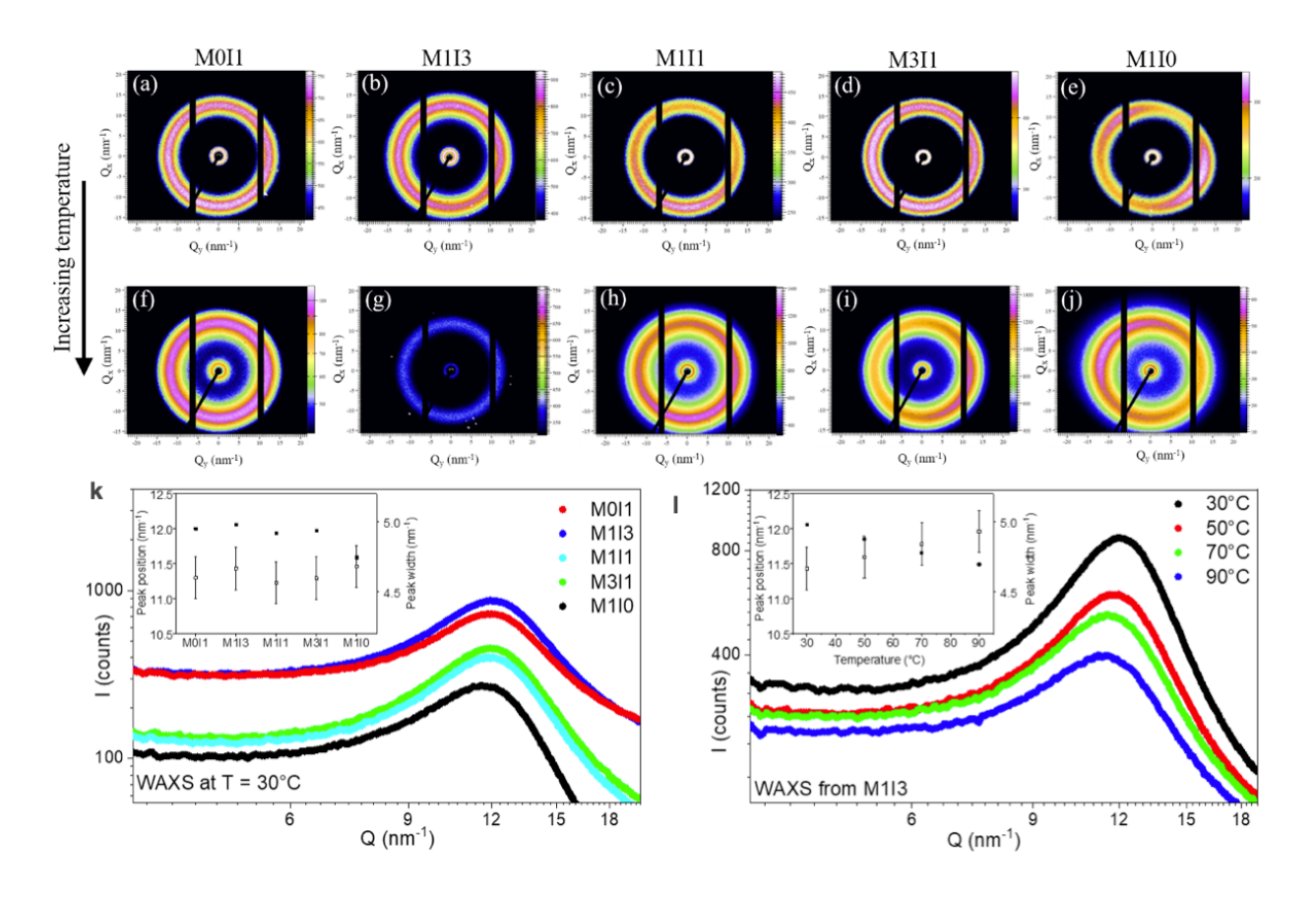


**Figure: 2: WAXS analysis: a-j,** 2D WAXS data for all five polymer samples (labelled), taken at 30 °C (upper row) and 90 °C (lower row). The black lines, where scattering data are unavailable, are from the beam stop and gaps between the detector modules;  $\mathbf{k}$ , Azimuthally integrated 1D intensity profiles for all polymer samples at a fixed temperature, T=30°C showing a prominent WAXS peak for all polymers. The inset shows peak position (filled squares) and peak width (empty squares), extracted from fits to the data, for each polymer;  $\mathbf{I}$ , 1D WAXS profile for the exemplary M1I3 polymer sample as a function of temperature from 30°C to 90°C. The WAXS peak, initially at Q=12.05 nm<sup>-1</sup> at 30°C broadens and shifts to a lower Q value = 11.49 nm<sup>-1</sup> after heating the polymer to 90°C.

The inset shows peak position (filled squares) and peak width (empty squares), extracted from fits to the data, for each temperature.

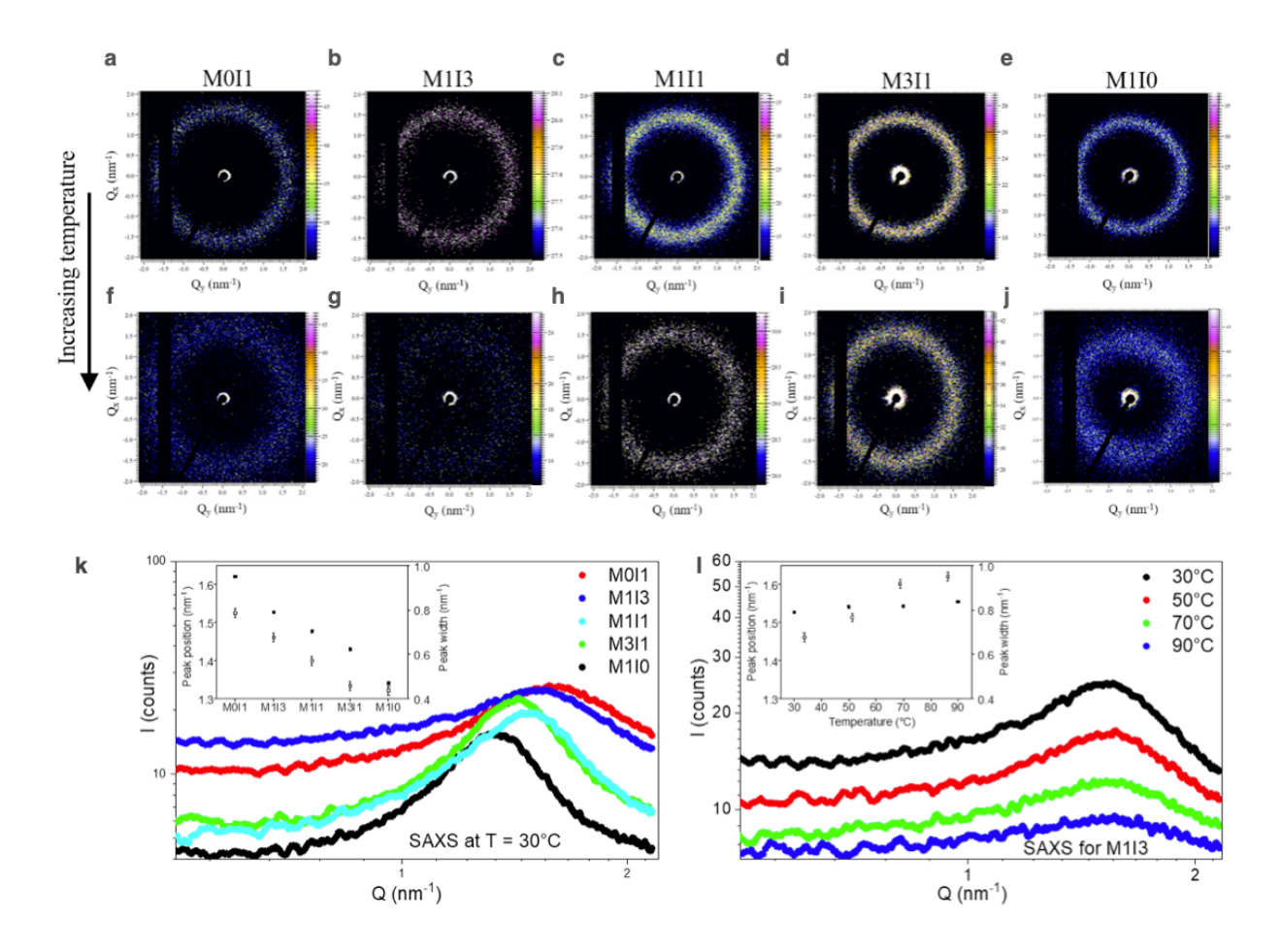


**Figure 3: SAXS analysis: a-j,** 2D SAXS data for all five polymer samples (labelled), taken at 30°C (upper row) and 90°C (lower row); **k**, 1D SAXS profiles for all polymer samples at a fixed temperature, T=30°C. The SAXS peak is narrowest for the most-rigid polymer M1I0 and broadens with decrease in M unit content and is the broadest for the most-flowable polymer sample M0I1. The inset shows peak position (filled squares) and peak width (empty squares), extracted from fits to the data, for each polymer; **I**, 1D SAXS profile for the exemplary M1I3 polymer sample as a function of temperature from 30°C to 90°C. The SAXS peak, initially at Q = 1.52 nm<sup>-1</sup> at 30° C broadens after heating the

polymer to  $90^{\circ}$ C and shifts to  $1.55~\text{nm}^{\text{-}1}$ . The inset shows peak position (filled squares) and peak width (empty squares), extracted from fits to the data, for each temperature.

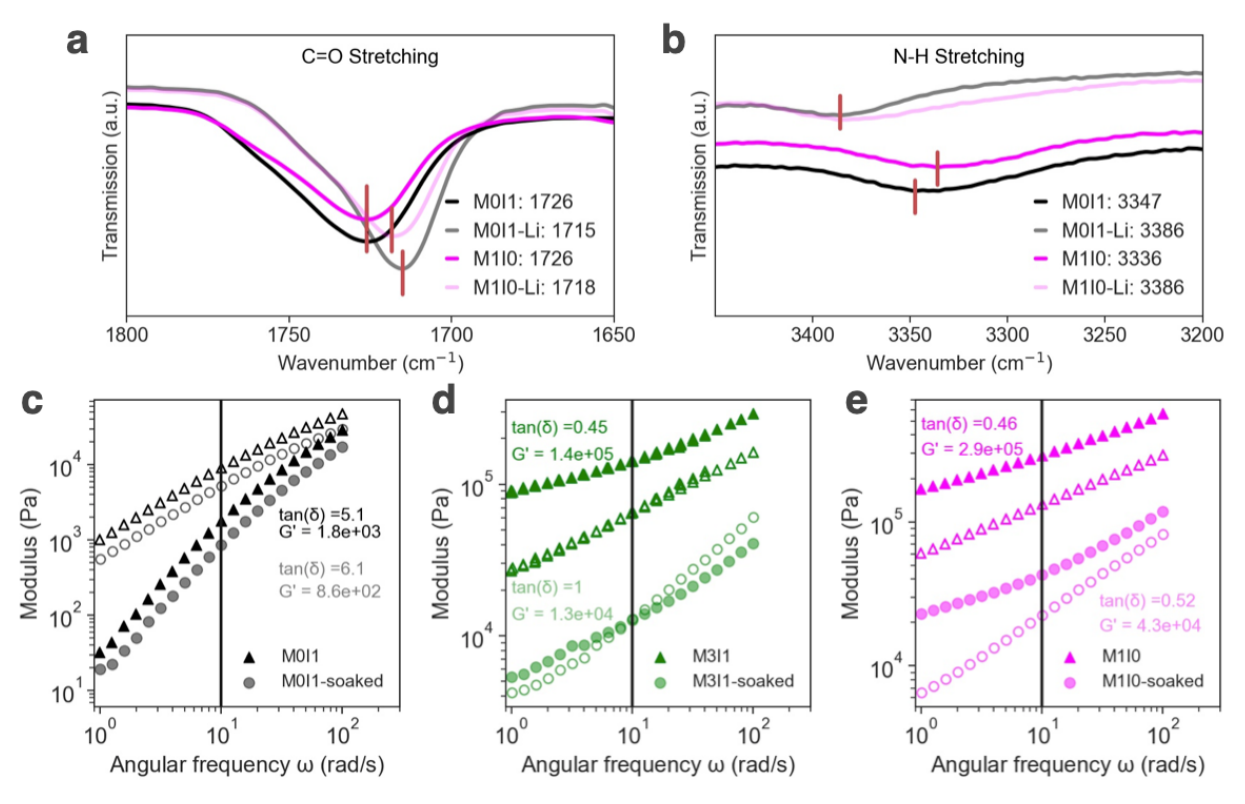


**Figure 4:** Polymer and salt interaction, FTIR spectrum of M0I1 and M1I0 polymer with and without LiTFSI added: **a**, C=O stretching; **b**, N-H stretching. The amount of LiTFSI is 1:1 molar ratio to either M or I linker; the rheological frequency sweep measured at 25 °C of the polymer after soaking in EC/DEC electrolyte for 2 hours: **c**, M0I1; **d**, M3I1; **e**, M1I0.

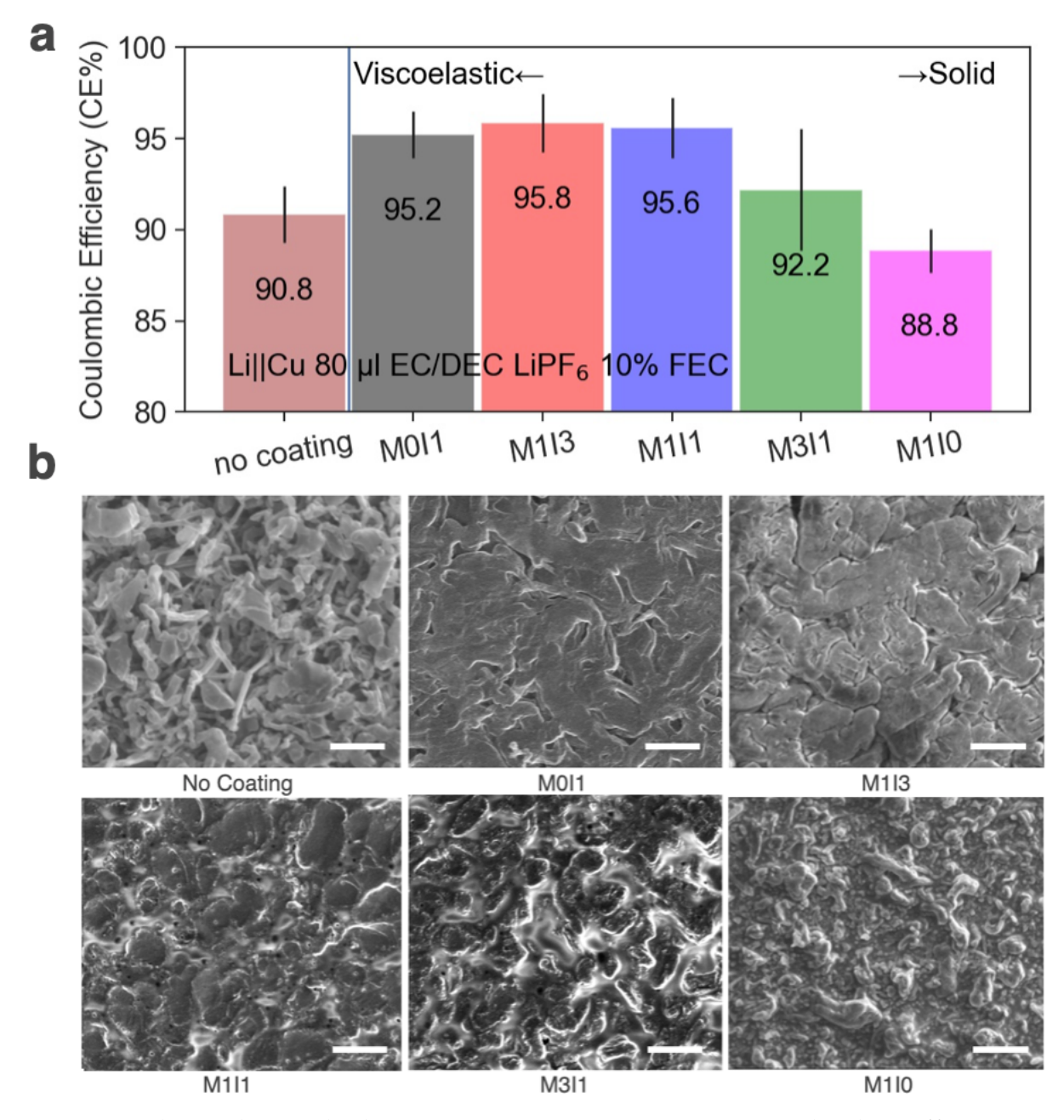


**Figure 5:** Electrochemical characterizations, **a**, comparing coulombic efficiency of electrodeposition for the bare and polymer coated copper electrodes (n=3). The current density utilized was 0.5 mA/cm<sup>2</sup>; **b** Morphology of electrodeposition on copper electrode with and without polymer coatings. Lithium was deposited at 0.5 mA/cm<sup>2</sup> for 2 hours. Here, the electrolyte utilized was 1 M LiPF<sub>6</sub> EC/DEC with 10 % FEC.

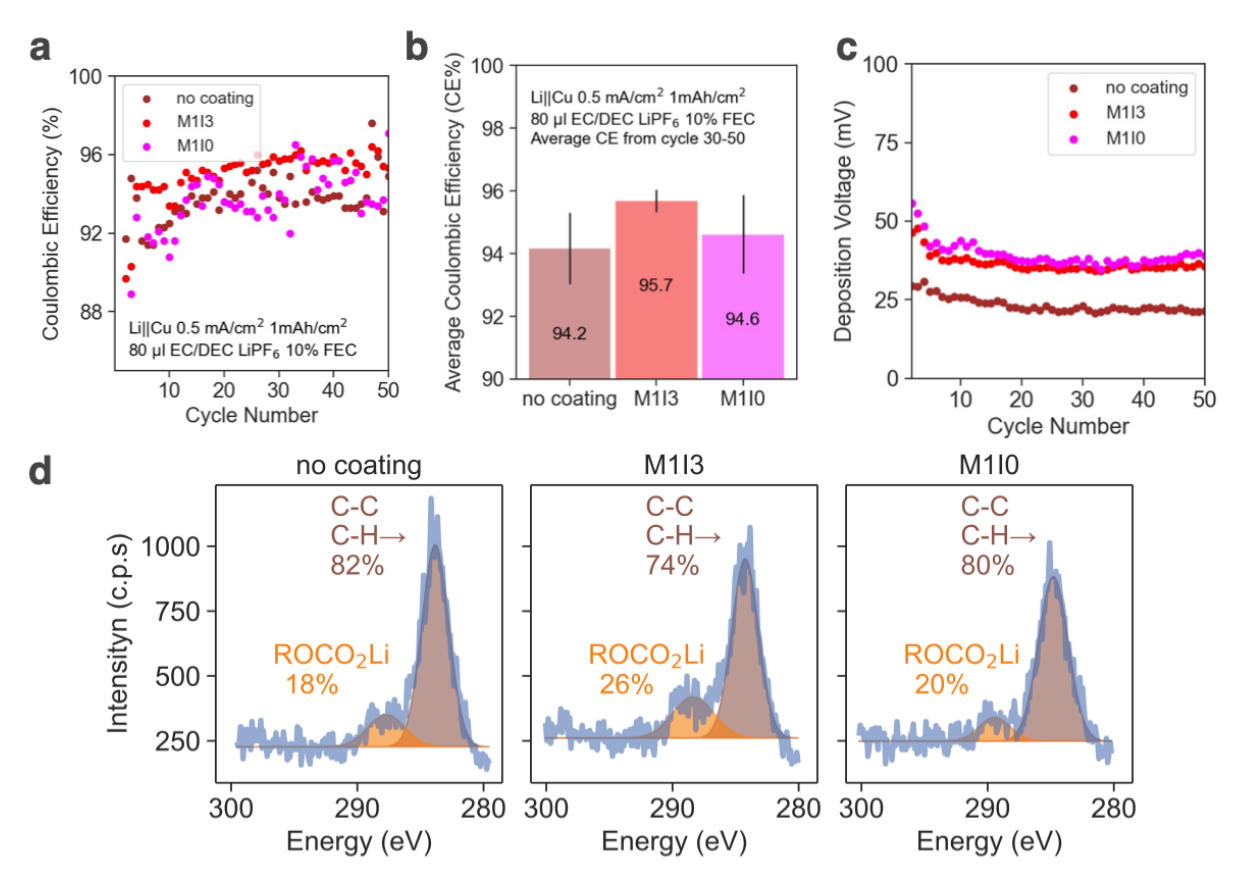


**Figure 6:** Electrochemical characterizations, **a**, long term CE measurement on Li | | Cu cells with cell parameters listed in the figure; **b**, the average CE from 30-50 cycles; **c**, absolute values of median lithium deposition voltages over cycles at different coating conditions; **d**, C1s spectrum of the SEI formed on Cu foil after 50 cell cycles.

## References

Amanchukwu, C. V *et al.* (2019) 'Nonpolar Alkanes Modify Lithium-Ion Solvation for Improved Lithium Deposition and Stripping', *Advanced Energy Materials*, 0(0), p. 1902116. doi: 10.1002/aenm.201902116.

Amanchukwu, C. V *et al.* (2020) 'A New Class of Ionically Conducting Fluorinated Ether Electrolytes with High Electrochemical Stability', *J. Am. Chem. Soc.* 

Bai, P. et al. (2016) 'Transition of lithium growth mechanisms in liquid electrolytes', Energy & Environmental Science, 9(10), pp. 3221–3229. doi: 10.1039/C6EE01674J.

Brissot, C., Rosso, M. and Lascaud, S. (1999) 'Dendritic growth mechanisms in lithiumrpolymer cells', *Journal of Power Sources*, 81–82, pp. 925–929.

Chen, L. *et al.* (2018) 'PEO/garnet composite electrolytes for solid-state lithium batteries: From "ceramic-in-polymer" to "polymer-in-ceramic", *Nano Energy*, 46, pp. 176–184. doi: https://doi.org/10.1016/j.nanoen.2017.12.037.

Chen, W.-J. *et al.* (2020) 'A Mixed Ether Electrolyte for Lithium Metal Anode Protection in Working Lithium–Sulfur Batteries', *ENERGY & ENVIRONMENTAL MATERIALS*, 3(2), pp. 160–165. doi: https://doi.org/10.1002/eem2.12073.

Cheng, X.-B. *et al.* (2017) 'Toward Safe Lithium Metal Anode in Rechargeable Batteries: A Review', *Chemical Reviews*, 117(15), pp. 10403–10473. doi: 10.1021/acs.chemrev.7b00115.

Chintapalli, M. *et al.* (2017) 'Incipient microphase separation in short chain perfluoropolyether-block-poly(ethylene oxide) copolymers', *Soft Matter*, 13(22), pp. 4047–4056. doi: 10.1039/C7SM00738H.

Choudhury, S. *et al.* (2015) 'A highly reversible room-temperature lithium metal battery based on crosslinked hairy nanoparticles', *Nat. Commun.*, 6, p. 10101.

Choudhury, S. *et al.* (2016) 'Hybrid Hairy Nanoparticle Electrolytes Stabilizing Lithium Metal Batteries', *Chemistry of Materials*, 28(7), pp. 2147–2157. doi: 10.1021/acs.chemmater.6b00029.

Choudhury, S. et al. (2017) 'Electroless Formation of Hybrid Lithium Anodes for Fast Interfacial Ion Transport', *Angewandte Chemie International Edition*, 56(42), pp. 13070–13077. doi: 10.1002/anie.201707754.

Choudhury, S. *et al.* (2018) 'Confining electrodeposition of metals in structured electrolytes', *Proceedings of the National Academy of Sciences*, 201803385.

Choudhury, S. *et al.* (2019) 'Solid-state polymer electrolytes for high-performance lithium metal batteries', *Nature communications*, 10(1), p. 4398. doi: 10.1038/s41467-019-12423-y.

Cooper, C. B. *et al.* (2020) 'Multivalent Assembly of Flexible Polymer Chains into Supramolecular Nanofibers', *Journal of the American Chemical Society*, 142(39), pp. 16814–16824. doi: 10.1021/jacs.0c07651.

Cooper, C. B. et al. (2021) 'High Energy Density Shape Memory Polymers Using Strain-

Induced Supramolecular Nanostructures', *ACS Central Science*. doi: 10.1021/acscentsci.1c00829.

Croce, F., Sacchetti, S. and Scrosati, B. (2006) 'Advanced, lithium batteries based on high-performance composite polymer electrolytes', *Journal of Power Sources*, 162(1), pp. 685–689. doi: 10.1016/j.jpowsour.2006.07.038.

Ding, F. *et al.* (2013) 'Dendrite-Free Lithium Deposition via Self-Healing Electrostatic Shield Mechanism', *Journal of the American Chemical Society*, 135(11), pp. 4450–4456. doi: 10.1021/ja312241y.

Dunn, B., Kamath, H. and Tarascon, J.-M. (2011) 'Electrical energy storage for the grid: a battery of choices.', *Science (New York, N.Y.)*, 334(6058), pp. 928–35. doi: 10.1126/science.1212741.

Gao, Y. *et al.* (2019) 'Polymer–inorganic solid–electrolyte interphase for stable lithium metal batteries under lean electrolyte conditions', *Nature Materials*, 18(4), pp. 384–389. doi: 10.1038/s41563-019-0305-8.

Gao, Y. *et al.* (2020) 'Low-temperature and high-rate-charging lithium metal batteries enabled by an electrochemically active monolayer-regulated interface', *Nature Energy*, 5, pp. 534–542. doi: 10.1038/s41560-020-0640-7.

Gasperini, A. *et al.* (2019) 'Characterization of Hydrogen Bonding Formation and Breaking in Semiconducting Polymers under Mechanical Strain', *Macromolecules*, 52(6), pp. 2476–2486. doi: 10.1021/acs.macromol.9b00145.

Hu, J. *et al.* (2017) 'Flexible Organic–Inorganic Hybrid Solid Electrolytes Formed via Thiol–Acrylate Photopolymerization', *Macromolecules*, 50(5), pp. 1970–1980. doi: 10.1021/acs.macromol.7b00035.

Huang, Z. et al. (no date) 'A Cation-Tethered Flowable Polymeric Interface for Enabling Stable Deposition of Metallic Lithium', *Journal of the American Chemical Society*, 142(51), pp. 21393–21403. doi: 10.1021/jacs.0c09649.

Kim, M. S. *et al.* (2016) 'Fabricating multifunctional nanoparticle membranes by a fast layer-by-layer Langmuir-Blodgett process: application in lithium-sulfur batteries', *Journal of Materials Chemistry A*, 4(38), pp. 14709–14719. doi: 10.1039/C6TA06018H.

Kong, X. *et al.* (2020) 'Dendrite Suppression by a Polymer Coating: A Coarse-Grained Molecular Study', *Advanced Functional Materials*, 30(15), p. 1910138. doi: https://doi.org/10.1002/adfm.201910138.

Li, S. *et al.* (2018) 'Single-Ion Homopolymer Electrolytes with High Transference

Number Prepared by Click Chemistry and Photoinduced Metal-Free Atom-Transfer

Radical Polymerization', *ACS Energy Letters*, 3(1), pp. 20–27. doi:

10.1021/acsenergylett.7b00999.

Liang, X. et al. (2017) 'A facile surface chemistry route to a stabilized lithium metal anode', Nat. Energy, 2, p. 17119.

Lin, D., Liu, Y. and Cui, Y. (2017) 'Reviving the lithium metal anode for high-energy batteries', *Nature Nanotechnology*, 12(3), pp. 194–206. doi: 10.1038/nnano.2017.16.

Liu, J. *et al.* (2019) 'Pathways for practical high-energy long-cycling lithium metal batteries', *Nature Energy*, 4(3), pp. 180–186. doi: 10.1038/s41560-019-0338-x.

Liu, K., Pei, A., Lee, H. R., Kong, B., Liu, N., Lin, D., Liu, Y., Liu, C., Hsu, P., *et al.* (2017) 'Lithium Metal Anodes with an Adaptive "Solid-Liquid" Interfacial Protective Layer', *Journal of the American Chemical Society*, 139(13), pp. 4815–4820. doi: 10.1021/jacs.6b13314.

Liu, K., Pei, A., Lee, H. R., Kong, B., Liu, N., Lin, D., Liu, Y., Liu, C., Hsu, P. chun, *et al.* (2017) 'Lithium Metal Anodes with an Adaptive "Solid-Liquid" Interfacial Protective Layer', *Journal of the American Chemical Society*, 139(13), pp. 4815–4820. doi:

Liu, Q. *et al.* (2018) 'Opposing Effects of Side-Chain Flexibility and Hydrogen Bonding on the Thermal, Mechanical, and Rheological Properties of Supramolecularly Cross-Linked Polyesters', *Macromolecules*, 51(22), pp. 9294–9305. doi: 10.1021/acs.macromol.8b01781.

10.1021/jacs.6b13314.

Liu, W. *et al.* (2017) 'Enhancing ionic conductivity in composite polymer electrolytes with well-aligned ceramic nanowires', *Nature Energy*, 2(5), p. 17035. doi: 10.1038/nenergy.2017.35.

Lopez, J. et al. (2018) 'Effects of Polymer Coatings on Electrodeposited Lithium Metal', Journal of the American Chemical Society, 140(37), pp. 11735–11744. doi: 10.1021/jacs.8b06047.

Lopez, J. et al. (2019) 'Designing polymers for advanced battery chemistries', Nature

Reviews Materials, 4(5), pp. 312–330. doi: 10.1038/s41578-019-0103-6.

Miao, R. *et al.* (2014) 'Novel dual-salts electrolyte solution for dendrite-free lithium-metal based rechargeable batteries with high cycle reversibility', *Journal of Power Sources*, 271, pp. 291–297. doi: 10.1016/j.jpowsour.2014.08.011.

Miao, R. *et al.* (2016) 'A new ether-based electrolyte for dendrite-free lithium-metal based rechargeable batteries.', *Scientific reports*, 6(February), p. 21771. doi: 10.1038/srep21771.

Paul, G. et al. (2018) 'Combined solid-state NMR{,} FT-IR and computational studies on layered and porous materials', Chem. Soc. Rev., 47(15), pp. 5684–5739. doi: 10.1039/C7CS00358G.

Pieczonka, N. P. W. *et al.* (2013) 'Impact of lithium bis(oxalate)borate electrolyte additive on the performance of high-voltage spinel/graphite Li-ion batteries', *Journal of Physical Chemistry C*, 117, pp. 22603–22612. doi: 10.1021/jp408717x.

Pires, J. *et al.* (2015) 'Role of propane sultone as additive to improve the performance of lithium-rich cathode material at high potential', *RSC Adv.* doi: 10.1039/C5RA05650K.

Qian, J. *et al.* (2015) 'High rate and stable cycling of lithium metal anode.', *Nature communications*, 6, p. 6362. doi: 10.1038/ncomms7362.

Ren, X. *et al.* (2018) 'Localized High-Concentration Sulfone Electrolytes for High-Efficiency Lithium-Metal Batteries', *Chem*, 4(8), pp. 1877–1892. doi: https://doi.org/10.1016/j.chempr.2018.05.002.

Roberts, M. F. and Jenekhe, S. A. (1991) 'Site-specific reversible scission of hydrogen bonds in polymers: an investigation of polyamides and their Lewis acid-base complexes by infrared spectroscopy', *Macromolecules*, 24(11), pp. 3142–3146. doi: 10.1021/ma00011a017.

Rosso, M. *et al.* (2001) 'Onset of dendritic growth in lithium/polymer cells', *Journal of Power Sources*, 97–98, pp. 804–806. doi: 10.1016/S0378-7753(01)00734-0.

Singh, M. *et al.* (2007) 'Effect of Molecular Weight on the Mechanical and Electrical Properties of Block Copolymer Electrolytes', *Macromolecules*, 40(13), pp. 4578–4585. doi: 10.1021/ma0629541.

Suo, L. *et al.* (2018) 'Fluorine-donating electrolytes enable highly reversible 5-V-class Li metal batteries', *Proceedings of the National Academy of Sciences*, 201712895.

Tu, Z. et al. (2017) 'Designing Artificial Solid-Electrolyte Interphases for Single-Ion and High-Efficiency Transport in Batteries', *Joule*, 1(2), pp. 394–406. doi: 10.1016/j.joule.2017.06.002.

Tu, Z. et al. (2018) 'Fast ion transport at solid–solid interfaces in hybrid battery anodes', *Nature Energy*, 3, pp. 310–316. doi: 10.1038/s41560-018-0096-1.

Whittingham, M. (2012) 'History, Evolution, and Future Status of Energy Storage', *Proceedings of The IEEE - PIEEE*, 100, pp. 1518–1534. doi: 10.1109/JPROC.2012.2190170. Yang, Q. *et al.* (2021) 'C–F-rich oil drop as a non-expendable fluid interface modifier with low surface energy to stabilize a Li metal anode', *Energy Environ. Sci.*, 14(6), pp.

3621–3631. doi: 10.1039/D0EE03952G.

Yu, Z. et al. (2019) 'A Dynamic, Electrolyte-Blocking, and Single-Ion-Conductive Network for Stable Lithium-Metal Anodes', *Joule*, 3(11), pp. 2761–2776. doi: 10.1016/j.joule.2019.07.025.

Zeng, Z. et al. (2018) 'Non-flammable electrolytes with high salt-to-solvent ratios for Liion and Li-metal batteries', *Nature Energy*, 3(8), pp. 674–681. doi: 10.1038/s41560-018-0196-y.

Zhang, H. *et al.* (2018) 'Lithiophilic-lithiophobic gradient interfacial layer for a highly stable lithium metal anode', *Nature Communications*, 9(1), p. 3729. doi: 10.1038/s41467-018-06126-z.

Zhang, R. *et al.* (2018) 'Coralloid Carbon Fiber-Based Composite Lithium Anode for Robust Lithium Metal Batteries', *Joule*, 2(4), pp. 764–777. doi: 10.1016/j.joule.2018.02.001. Zhang, X.-Q. *et al.* (2017) 'Fluoroethylene Carbonate Additives to Render Uniform Li Deposits in Lithium Metal Batteries', *Advanced Functional Materials*, 27(10), p. 1605989. doi: 10.1002/adfm.201605989.

Zheng, G. *et al.* (2016) 'High-Performance Lithium Metal Negative Electrode with a Soft and Flowable Polymer Coating', *ACS Energy Letters*, 1(6), pp. 1247–1255. doi: 10.1021/acsenergylett.6b00456.

Zheng, J. et al. (2020) 'Regulating electrodeposition morphology of lithium: towards commercially relevant secondary Li metal batteries', Chemical Society Reviews, 49(9), pp.

2701-2750. doi: 10.1039/C9CS00883G.

Zheng, J., Tang, M. and Hu, Y.-Y. (2016) 'Lithium Ion Pathway within Li7La3Zr2O12-Polyethylene Oxide Composite Electrolytes', *Angewandte Chemie International Edition*, 55(40), pp. 12538–12542. doi: 10.1002/anie.201607539.